

Studying the metallicity gradient in Virgo Ellipticals with E-ELT photometry of resolved stars

L. Schreiber,^{1*} L. Greggio,² R. Falomo,² D. Fantinel² and M. Uslenghi,³

¹*INAF, Osservatorio Astronomico di Bologna, Via Ranzani 1, Bologna, 40127, Italy*

²*INAF, Osservatorio Astronomico di Padova, Vicolo dell'Osservatorio 5, Padova, 35122, Italy*

³*INAF, Istituto di Astrofisica Spaziale e Fisica Cosmica, Via Bassini 15, Milano, 20133, Italy*

Accepted 1988 December 15. Received 1988 December 14; in original form 1988 October 11

ABSTRACT

The next generation of large aperture ground based telescopes will offer the opportunity to perform accurate stellar photometry in very crowded fields. This future capability will allow one to study in detail the stellar population in distant galaxies. In this paper we explore the effect of photometric errors on the stellar metallicity distribution derived from the color distribution of the Red Giant Branch stars in the central regions of galaxies at the distance of the Virgo cluster. We focus on the analysis of the Color-Magnitude Diagrams at different radii in a typical giant Elliptical galaxy obtained from synthetic data constructed to exemplify observations of the European Extremely Large Telescope. The simulations adopt the specifications of the first light high resolution imager MICADO and the expected performance of the Multi-Conjugate Adaptive Optics Module MAORY. We find that the foreseen photometric accuracy allows us to recover the shape of the metallicity distribution with a resolution $\lesssim 0.4$ dex in the inner regions ($\mu_B = 20.5$ mag arcsec⁻²) and $\simeq 0.2$ dex in regions with $\mu_B = 21.6$ mag arcsec⁻², that corresponds to approximately half of the effective radius for a typical giant elliptical in Virgo. At the effective radius ($\mu_B \simeq 23$ mag arcsec⁻²), the metallicity distribution is recovered with a resolution of $\simeq 0.1$ dex. It will thus be possible to study in detail the metallicity gradient of the stellar population over (almost) the whole extension of galaxies in Virgo. We also evaluate the impact of moderate degradations of the Point Spread Function from the assumed optimal conditions and find similar results, showing that this science case is robust.

Key words: instrumentation: adaptive optics – methods: observational – galaxies: stellar content – stars: imaging.

1 INTRODUCTION

In spite of the general consensus on the hierarchical model for the formation of galaxies, the details on their growth and assembly are still unclear. For example, in the case of Elliptical galaxies, we do not know whether their assembly occurs preferentially via dry merging, involving mostly stars, or wet merging, involving stars and gas, accompanied by star formation (e.g. Ciotti et al. 2007). According to Kormendy et al. (2009), these two modalities could lead to a dichotomy in several properties of this kind of galaxies, including, e.g., the formation of disk ellipticals when wet merging is dominant, or boxy ellipticals in the opposite case, as well as other observational evidences (Ciotti 2009). Other scenarios consider the occurrence of wet merging preferentially at high redshift, followed by prevailing dry merging

at lower redshift (Oser et al. 2010). Alternatively, the formation process could be characterized by two main phases, with in-situ star formation producing the inner regions at early epochs, followed by the growth of the external parts of the galaxies via dry merging. In this model the importance of the latter mechanism increases with galaxy size. Different formation paths imprint upon different metallicity distributions and gradients over the galactic radii. For example, in the case of wet merging, the gas should deposit in the central regions of the accreting galaxy, where the last star formation episode would occur. This process leads to the construction of sizable metallicity gradients, with metal rich stars dominating the central parts of the galaxy. Conversely, a prevalence of dry merging would result into a quite flat metallicity gradient, the accreted galaxies being disrupted and their members mixed to the accretor's stars. Therefore, the observational determination of metallicity distributions

* E-mail: laura.schreiber@oabo.inaf.it

and metallicity gradients in Ellipticals provide strong constraints on their formation models.

This problem has been investigated through the analysis of integrated colors and line indices gradients in galaxies (e.g. Weijmans et al. 2009; Coccato et al. 2010; Rawle et al. 2010; Kim & Im 2013). These studies support the notion that dry merging is indeed important in the formation of ellipticals, but the actual size of the metallicity gradients and its trend with galaxy size are a matter of debate. In addition, the integrated light can only yield a global information on the metallicity, and this information is necessarily weighted by luminosity, which favors the younger stellar generations. Conversely, tight constraints on the formation models could be obtained from the detailed study of metallicity distribution, its peak and extension, and its trend with radius. An efficient way to measure the metallicity distribution function (MDF) involves the analysis of the color distribution of stars on the Red Giant Branch (RGB) (e.g. Harris et al. 1999). RGB stars are intrinsically very bright, and are produced by stellar populations with an extremely large range of ages, older than ~ 2 Gyr up to the Hubble time. Therefore, this component of the stellar population samples almost the whole star formation history of the galaxy. Although the color of the RGB stars also depends on their age, the sensitivity to metallicity is much more pronounced, so that the width of the RGB is often used to derive the width of the metallicity distribution of a stellar population.

Individual spectroscopy for bright RGB stars ($M_I \simeq -3.5$) cannot be performed even for the Ellipticals nearest to us, leaving the photometric method as the only means to access the metallicity distribution. A thorough study of this kind has been performed for the nearby elliptical galaxy Centaurus A (Harris & Harris 2000; Rejkuba et al. 2005), through the analysis of CMDs obtained from HST data in different regions of the galaxy, sampling the stellar populations from $\simeq 8$ to $\simeq 38$ Kpc from the center. The results show that the metallicity distribution is very wide in all the examined fields, with very little variations of the peak and width. However, single star photometry in the inner regions is hampered by crowding; the innermost field studied in Centaurus A is located at 8 Kpc from the center, corresponding to 1.5 times the effective radius (R_{eff}), leaving unexplored most of the stellar mass of the galaxy.

With the exquisite resolving power of the future 40 m class European-Extremely Large Telescope (E-ELT) (Gilmozzi & Spyromilio 2007) working close to the diffraction limit, thanks to the Laser Guide Stars (LGS) assisted Multi-Conjugate Adaptive Optics (MCAO), it will be possible to perform accurate photometry of bright RGB stars in extremely crowded fields, down to the inner regions of galaxies and to map the metallicity distribution over the whole Ellipticals. With the E-ELT we will be able to study galaxies beyond the Centaurus group, and in particular access members of the Virgo Cluster, enabling the comparison of the metallicity distribution in a suitable sample of galaxies located in different environments.

This paper builds on Greggio et al. (2012) in which this problem was explored, leading to the encouraging result that the uncertainty on the metallicity of a bright RGB star amounts to ~ 0.1 dex at approximately 0.5 effective radii in a typical elliptical in Virgo. Here we expand the investigation to quantify how the accuracy varies with star crowding,

from the central parts, up to $\sim 2 R_{\text{eff}}$. Moreover, we add the discussion of the effect on the results of the small variations of the Point Spread Function (PSF) across the whole MICAADO (Multi-AO Imaging Camera for Deep Observations) Field of View (FoV) due to the non-uniformity of the MCAO correction and to variation of seeing conditions.

The expected performance of an ELT for photometry in crowded fields has been investigated by Olsen, Blum & Rigaut (2003) and Deep et al. (2011). These papers aim at quantifying in general the photometric accuracy and its variation with crowding. Here we address a specific scientific issue, assessing the accuracy with which the metallicity distribution can be derived, which degrades with crowding. The paper is organized as follows. In Sect. 2 we describe how the simulated frames were produced, detailing in particular the adopted PSF (Sect. 2.3), while in Sect. 3 we exemplify how the synthetic images were reduced. In Sect. 4 we report our results: the quality of the photometric measurements (Sect. 4.1), the derived CMDs (Sect. 4.2), and the MDF resulting from the analysis of the RGB stars (Sect. 4.3). The comparison of this MDF to the input one clearly illustrates the feasibility of the considered science case. In Sect. 5 we discuss how the results change when considering a non-optimal PSF. A summary of our results is presented in Sect. 6.

2 SIMULATED DATA

2.1 The science case

In this paper we focus on the problem of deriving the stellar metallicity distribution in different parts of a giant elliptical galaxy member of the Virgo Cluster by means of simulated star fields. At a distance of 18 Mpc, the brightest stars of an old stellar population, which are at the Tip of the RGB, have $J \simeq 26$ mag. For our simulations we adopt the same model stellar population as in Greggio et al. (2012), namely a flat age distribution between 10 and 12 Gyr, and a metallicity distribution determined for a halo field in the elliptical galaxy Centaurus A (Rejkuba et al. 2005) (see Fig. 1). We refer the reader to Greggio et al. (2012) for details on the model computations; we recall here only some properties of the stellar population: the ratio between the mass of formed stars and current B band luminosity is $7.05M_{\odot}/L_{B,\odot}$; integrated colors are $B - V = 0.88$; $B - I = 1.97$; $B - K = 3.66$.

On the CMDs of Fig. 1, the different metallicity bins appear well separated, thereby illustrating the diagnostic of the color of RGB stars. Comparing the left to the central panel one can appreciate the superior sensitivity to metallicity of the $I - J$ with respect to the $J - K$ color, because the wider wavelength baseline better traces the stellar effective temperature. The quality of the metallicity distribution derived from the CMD will depend on the photometric errors affecting the color distribution of the stars, that depend on crowding conditions. We map quantitatively this effect by placing the stellar population at different locations within the galaxy, i.e. at different surface brightness levels. Real galaxies could be characterized by a systematic trend of the metallicity distribution with galactic radius; however we do not attempt to incorporate this variation in our modeling, since we aim at evaluating how crowding affects our

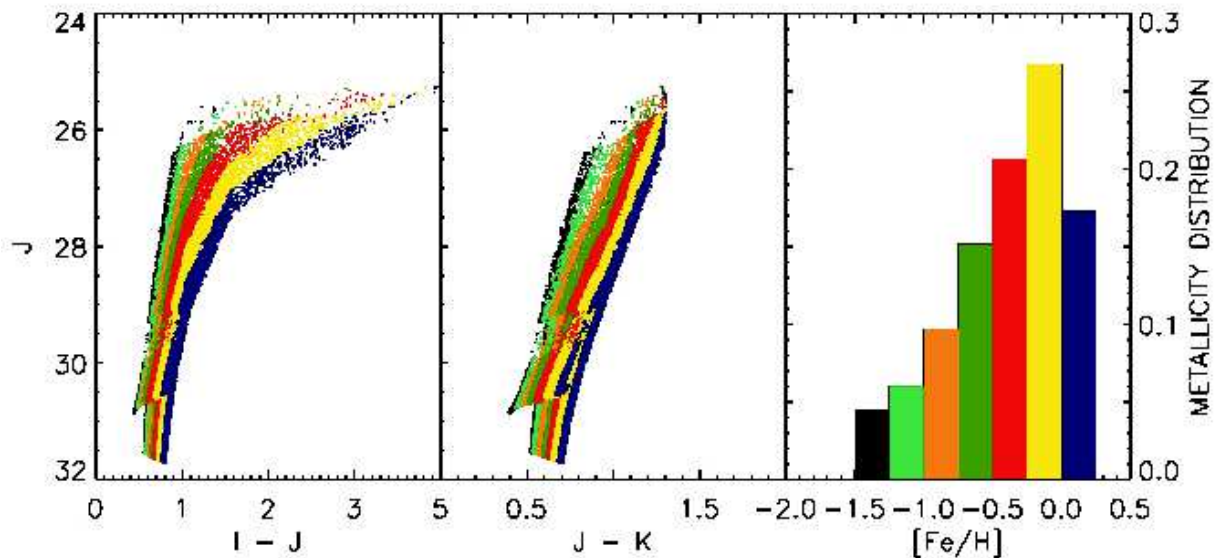


Figure 1. The optical Near-IR CMDs (left and central panels) and the metallicity distribution (right panel) of the model stellar population considered for our science case. On the CMDs dots are colored according to their metallicity with the same encoding as in the right panel. The simulation is the same as in Greggio et al. (2012), and corresponds to a total mass of $6.8 \cdot 10^7 M_{\odot}$ of stars formed between 10 and 12 Gyr ago. The synthetic CMD has been computed with the YZVAR code by G.P. Bertelli using the Girardi et al. (2002) stellar tracks. Please note that the sharp boundaries between the populations are due to the solid colors used for the dots of the plots. Actually there is a partial overlap of the RGB loci occupied by stars members of adjacent metallicity bins, which is not visible in the figure.

capability of recovering a given metallicity distribution from photometry of the resolved stars in the galaxy.

2.2 The instrument

The first light imaging system currently foreseen for the future 40 m class E-ELT will consist of a high resolution camera (MICADO, Davies et al. 2010) coupled with MAORY (Multi-conjugate Adaptive Optics Relay Diolaiti et al. 2010), an LGS assisted MCAO module.

The MICADO camera, optimized for imaging at the diffraction limit, will fully sample the 6 (11) mas PSF core FWHM in the J (K) bands; it requires an image correction of high quality and uniformity across a FoV of 53×53 arcsec on the wavelength range $0.8 - 2.4 \mu\text{m}$. A good uniformity of the high resolution PSF across the FoV is ensured by the MAORY MCAO module by means of several deformable mirrors, optically conjugated to different turbulent layers, and several guide stars, to obtain a kind of 3-dimensional mapping of the turbulence. The MAORY phase A baseline takes advantage of a constellation of 6 LGS and 3 Natural Guide Stars (NGS) for the turbulence sensing, following the choice adopted in other MCAO systems for present and future telescopes, like GeMS on Gemini (Neichel et al. 2010) and NFIRAOS (Herriot et al. 2010) on the future Thirty Meter Telescope (TMT, Szeto et al. 2008). MCAO was successfully demonstrated on-sky by the Multi conjugate Adaptive optics Demonstrator (MAD) on the Very Large Telescope (e.g. Marchetti et al. 2008; Gullieuszik et al. 2008; Fiorentino et al. 2011) and by GeMS on Gemini (Rigaut et al. 2012).

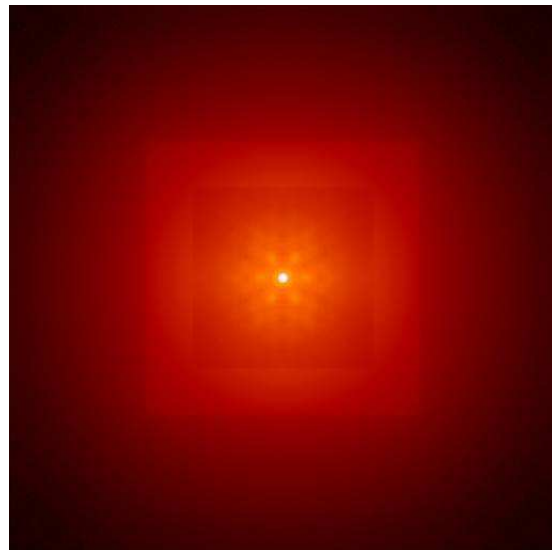


Figure 2. The MAORY PSF complex shape, characterized by a sharp core and an extended and highly structured halo. The side of the FoV of the Fig. is ~ 1.5 arcsec.

2.3 Input Point Spread Functions

The PSFs for the synthetic images have been downloaded from the MAORY official website¹. The MAORY PSF (Fig. 2 shows an example in the J band) presents a very complex shape, where the main central component has the

¹ <http://www.bo.astro.it/maory/Maory/Welcome.html>

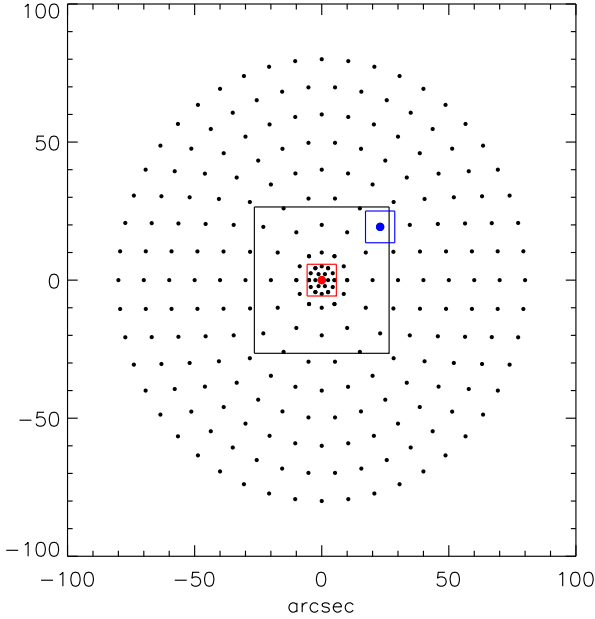


Figure 3. Polar grid of computed PSFs positions across the MAORY FoV. The central black square indicates the 53×53 arcsec MICADO FoV. Colored dots mark the positions of the two PSFs considered to evaluate the dependence of the results from spatial PSF variations. The colored squares show the size of the widest of our simulated images.

typical shape of the Airy disk, and the secondary structures can be attributed to the MCAO system characteristics. The secondary peaks arranged in a quasi-hexagonal configuration mirror the constellation of the 6 LGSs; the big external square reflects the density and the displacement of the deformable mirrors actuators, and the external halo is produced by residual light due to the non-perfect correction of the turbulence.

In order to map the PSF variations across the FoV, model PSFs are computed on a polar grid of directions (shown in Fig. 3). For each photometric band and point of the grid they are available for two seeing atmospheric conditions: “median seeing” condition (FWHM = 0.8 arcsec at $0.5 \mu\text{m}$) and “good seeing” condition (FWHM = 0.6 arcsec). Fig. 4 shows the trend of the predicted MAORY PSF Strehl Ratio (SR) with distance from the center of the FoV. The SR is the ratio of the maximum intensity in the PSF to that in the theoretically perfect point source image (Airy disk) and it is a tracer of the image quality after AO correction. The performance across the MICADO FoV is remarkably uniform, due to the multi-conjugation of the AO correction.

Fig. 2.3 shows two examples of the model MAORY PSF in the J band under “good seeing” conditions, in the two locations on the FoV shown in Fig. 3 by the two colored filled circles. Fig. 2.3 exemplifies the maximum expected variation of the PSF on the MICADO FoV. We explore the sensitivity of our results on PSF variations by computing two sets of simulated images, adopting the model “good seeing” PSFs in the two locations shown in Fig. 3. In addition, we compute a third set of frames using the “median seeing” PSF in the center of the FoV. Since the PSF variation across the whole

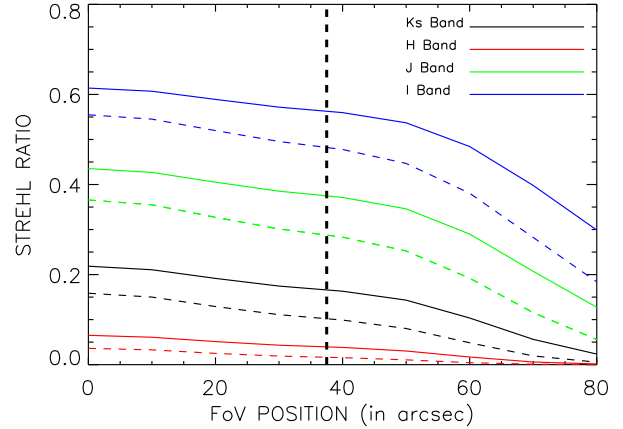
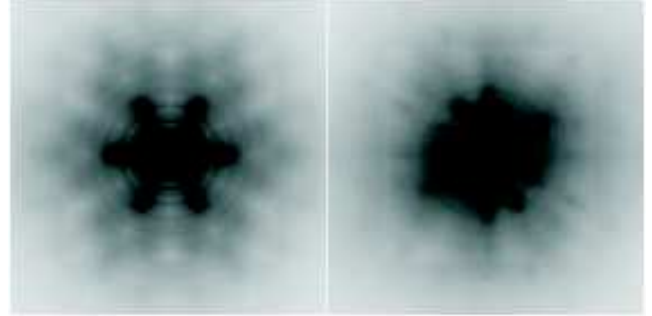


Figure 4. Radial profile averaged over the FoV (from the center of the MAORY FoV up to a radial distance of 80 arcsec) of the predicted SR value for the K_s , H , J and I bands and for a seeing value of 0.6 arcsec (continuous lines) and 0.8 arcsec (dashed lines). The vertical thick dashed line represents the distance from the center to the corner of the MICADO FoV. This plot depicts the typical behavior of the SR when AO is employed: the best correction level and image quality is reached at the center of the FoV, both degrading as the radial distance increases.



MICADO FoV is very low, we assumed a fixed PSF for each simulated frame.

2.4 Frames generation

The images have been simulated using the AETC tool² (Falomo, Fantinel & Uslenghi 2011) with the E-ELT MICADO configuration. We recall in Table 1 all the relevant parameters of the telescope and of the instrument we have considered, as well as the observation conditions. We simulated images in the I , J , H and K_s bands for the science case described in Sect. 2.1 at different surface brightness levels (i.e. crowding conditions) and scaling the image FoV. The characteristics of the various cases considered are summarized in Table 2. The total B band luminosity of the stellar population sampled by the synthetic frame is given by:

$$L_B = FoV^2 10^{-0.4*(\mu_B - M_{B,\odot} - DM)} L_{B,\odot} \quad (1)$$

where FoV^2 is the area of the simulated frame in arcsec^2 ,

² The Advanced Exposure Time Calculator, AETC; <http://aetc.oapd.inaf.it/>

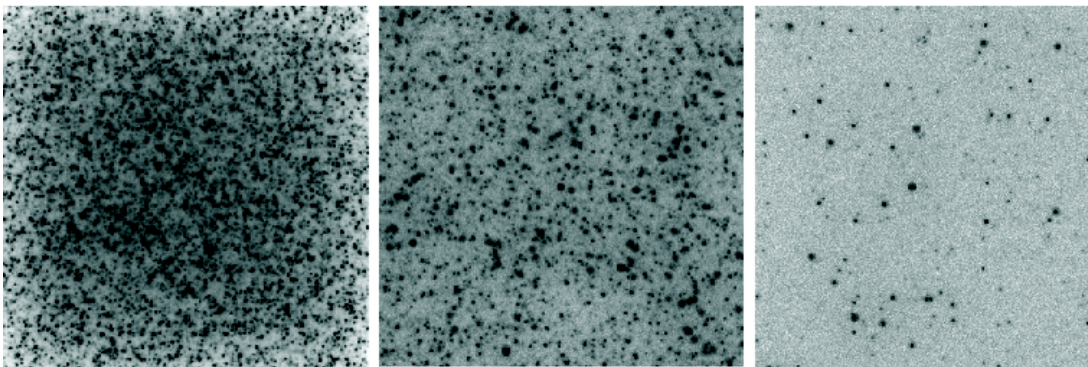


Figure 5. Simulated images of a 1×1 arcsec stellar field in the J band with three different levels of surface brightness. The images adopt the central, “good” seeing PSF and refer to $\mu_B = 19.3$ (left panel), $\mu_B = 21.64$ (central panel) and $\mu_B = 24.54$ mag arcsec $^{-2}$ (right panel), that correspond to the μ_B characteristic at 0.1, 0.5 and 2 effective radii respectively of an Elliptical galaxy in Virgo. The simulated images total integration time is 2 hours.



Figure 6. The central region of the MAORY PSF in the J band compared to the PSFs extracted from the simulated frames by StarFinder varying the crowding condition. Starting from the left we have: (1) the input MAORY PSF in the J band (central 100×100 pixels region corresponding to 300×300 mas); (2) the PSF extracted from a simulated frame with $\mu_B = 19.3$ mag arcsec $^{-2}$; (3) the PSF extracted from a simulated frame with $\mu_B = 21.64$ mag arcsec $^{-2}$; (4) the PSF extracted from a simulated frame with $\mu_B = 24.54$ mag arcsec $^{-2}$.

Table 1. Relevant parameters of the telescope and of the instrument given to the simulator to generate the synthetic frames. We assumed the typical Near-IR sky background at Paranal (Chile) and included the contribution of thermal emission in the Near-IR bands.

| | |
|-------------------------|------------------------|
| Collecting Area | 1100 m 2 |
| Read Out Noise | 5 e^- |
| Plate-Scale | 3 mas |
| Throughput | |
| (I, J, H, K_s bands) | 0.4, 0.39, 0.4, 0.39 |
| Sky background mag | |
| (I, J, H, K_s bands) | 20.1, 16.3, 15.0, 12.8 |

μ_B is the (un reddened) surface brightness of the stellar population, DM is the distance modulus. We adopt DM = 31.3 mag and a solar absolute magnitude of $M_{B,\odot} = 5.48$. The number of stars populating a given section of the CMD is proportional to L_B . In order to maintain the same statistical sampling of the CMD in all the explored cases, we chose FoV and μ_B to produce fields with constant $L_B \simeq 10^7 L_{B,\odot}$. The explored cases encompass a wide range of surface brightness (SB), almost down to the center of a typical giant elliptical galaxy at the distance of the Virgo cluster (see Table 2). Stars brighter than a threshold magnitude (~ 1.5 mag fainter than the limiting magnitude (S/N=5) of the

Table 2. Summary of the analyzed cases. Column (2): surface brightness in the B band in mag per arcsec 2 ; column (3): size of the simulated square frame in arcsec; column (4): fraction of the galaxy effective radius corresponding to the specific SB for a Devacoleur profile of a galaxy with $M_B = -22$ at a distance of 18 Mpc. Notice that the surface brightness in other photometric bands can be obtained from that in the B band by applying the integrated colors of the stellar population: $B - V = 0.88$, $B - I = 1.97$, $B - K_s = 3.66$; column (5): number of simulated sources for each frame.

| Case | μ_B | FoV | R/ R_{eff} | # of stars |
|------|---------|-------|---------------------|------------|
| 1 | 19.3 | 1.03 | 0.1 | 124533 |
| 2 | 20.54 | 1.8 | 0.25 | 125581 |
| 3 | 21.06 | 2.29 | 0.35 | 126108 |
| 4 | 21.64 | 3.01 | 0.5 | 125552 |
| 5 | 22.26 | 4 | 0.7 | 126128 |
| 6 | 22.97 | 5.54 | 1 | 126002 |
| 7 | 23.85 | 8.34 | 1.5 | 125997 |
| 8 | 24.54 | 11.45 | 2 | 126083 |

simulation) are used for the simulated frames, while the remaining light of the stellar population is distributed over the frame as a pedestal, with its associated Poisson noise. This ensures that the effect of blending of stellar images is well characterized also at the faint end of the luminosity func-

tion. For the considered science case, the input stellar lists, used to generate the frames, contain ≈ 126000 stars brighter than $K = 31$ mag (Table 2). This number of synthetic stars proved to be large enough to ensure a good statistical sampling of the photometric error. The lists include information on mass, age, metallicity, magnitudes in the I , J , H and K_s bands and the coordinates on the frame of each star. Synthetic frames are generated from these lists in the corresponding bands with the following steps: for each star, the properly re-sampled MAORY PSF is positioned on the coordinates; the source flux is computed by the AETC with the MICADO configuration assuming an exposure time of 2 hours (adding 100 individual exposures); the photon noise statistic is added taking into account the subtraction of the background due to the telescope and to the sky + the non-resolved stars component; finally the total Read Out Noise is added. Fig. 5 shows three simulated images obtained assuming different surface brightness values and illustrate the explored range of crowding conditions.

3 PHOTOMETRIC ANALYSIS

The synthetic frames are characterized by highly structured PSFs, with sharp diffraction limited core and extended halo (see Figure 2.3). The complex shape of the PSF, typically obtained when AO is involved, can not be easily represented by a simple combination of few analytical components (Schreiber et al. 2012). We therefore decided to perform the PSF photometry using the StarFinder code (Diolaiti et al. 2000), a program specifically designed for high resolution AO images taking into account the problem of reliable stars recognition in crowded fields with a highly structured PSF. The analysis is accomplished by PSF fitting, using a numerical PSF template extracted from the frame, in order to account for all the bumps and fine scale structures. StarFinder estimates first the background, that can be variable across the frame, and the noise standard deviation. The candidate stars are then chosen by selecting the sources with a peak value statistically significant above the background, they are listed by decreasing intensity and they are compared to the PSF through cross-correlation, yielding an objective measure of similarity. If the correlation coefficient is higher than a pre-fixed threshold, the object is rated similar to the PSF and accepted. The accurate determination of its position and flux are obtained by means of a local fit. We set a detection threshold of 3σ , where σ stands for the background noise standard deviation, and a correlation coefficient of 0.5. The contribution of the detected stars is recorded into an image model which is continuously updated and used as a reference to account for the contamination of the already detected sources. After a first iteration of the star detection loop with a preliminary rough photometric analysis, the contaminating sources around the stars selected for the PSF estimation are identified and the initial background estimation gets refined, resulting in a more accurate PSF estimation. Figure 6 shows the central part of the MAORY PSF in the J band and the PSFs extracted by StarFinder from three simulated frames with different crowding conditions. It is noteworthy how the halo details are better recovered as the surface brightness, and so crowding, decreases. The StarFinder code is written in IDL language and the cur-

Table 3. Fraction of spurious detections.

| μ_B | Fraction in % | | | |
|---------|---------------|------|------|-------|
| | I | J | H | K_s |
| 19.3 | 0.03 | 0.06 | 0.08 | 0.4 |
| 20.54 | 0.08 | 0.4 | 1.3 | 2.5 |
| 21.06 | 0.2 | 0.7 | 1.5 | 2.2 |
| 21.64 | 0.4 | 0.7 | 1.7 | 2.6 |
| 22.26 | 0.4 | 0.6 | 1.2 | 1.4 |
| 22.97 | 0.3 | 0.6 | 0.9 | 1.0 |
| 23.85 | 0.3 | 0.3 | 0.4 | 0.5 |
| 24.54 | 0.3 | 0.3 | 0.3 | 0.3 |

rent version, provided with a widget-based Graphical User Interface, is open-source and available on-line³.

4 RESULTS

4.1 Photometric accuracy and completeness

The photometric accuracy is evaluated for each band and for each crowding condition, matching the input and output catalogues. The chosen matching algorithm searches for candidate counterparts within 1 pixel distance to each detected source and, in case of ambiguity due to multiple candidates, the brightest star is chosen. No limit between the input and output magnitude difference has been set. This criterion has the merit of being independent of the magnitude difference between the input and output source, that is what we want to measure. However it has the drawback of inducing false associations of very faint stars with relatively bright detected objects. This spurious association occurs in particular at high surface brightness levels, when the number of faint stars in the error box around the detected source is large. At the other extreme, when no input source is found within 1 pixel distance, the detected source is considered as a spurious detection, due to noise spikes or to inaccurate PSF modeling. Notice that the secondary peaks of the structured MAORY PSF (outlined in Fig. 2 and Fig. 2.3) may induce false detection of faint stars if the extracted PSF lacks details in the halo substructures. In this respect, the numerical PSF extracted by StarFinder provides a high quality modeling of the halo sub-structures that limits this problem. Table 3 shows that most of the spurious detections are due to noise spikes, especially in high crowding conditions, and the percentage of spurious objects is larger for redder wavelengths because the higher background level generates more spikes. The largest fractions of spurious detections occur for $\mu_B = 21.64$ mag arcsec⁻², which corresponds to an intermediate level of crowding among the analyzed cases. For very high crowding the adopted matching criterion, which only relies on the position of the sources, maximizes the association between an output and an input star, thereby minimizing the cases in which an output star has no counterpart in the input list. All the simulated images included ≈ 126000 stars with $K_s \leq 31$ mag (see Table 2). The number of detected sources for each case and in each band is reported in Table 4. The detection of sources is limited by two main

³ <http://www.bo.astro.it/StarFinder>

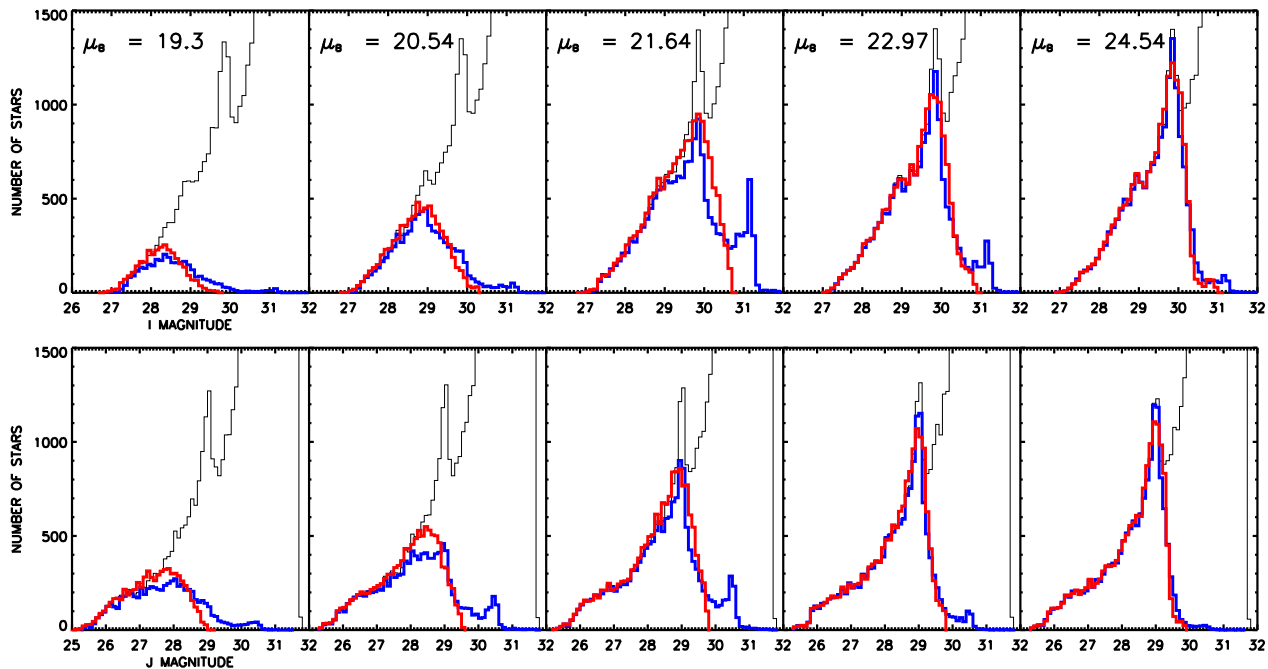


Figure 7. Input and output luminosity functions in the I (top) and J (bottom) bands varying the crowding conditions (decreasing crowding for left to right). Thin lines show the input luminosity functions; thick red lines highlight the output luminosity functions; thick blue lines show the luminosity function of input stars which have been position matched to a source in the output catalogue according to our algorithm. The discrepancy between the red and blue histograms is mainly due to crowding.

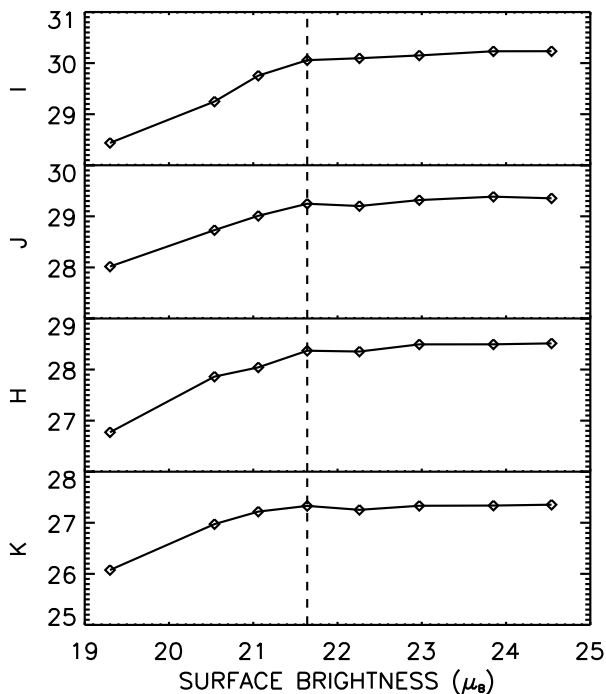


Figure 8. The 50 per cent completeness magnitude as a function of the surface brightness for the various bands. Note that at $\mu_B \gtrsim 21.5$ the completeness magnitude becomes independent of surface brightness in all bands.

Table 4. Number of detected sources.

| μ_B | Detected sources | | | |
|---------|------------------|-------|-------|------|
| | I | J | H | Ks |
| 19.3 | 3234 | 6915 | 4705 | 3310 |
| 20.54 | 7471 | 11402 | 10472 | 5931 |
| 21.06 | 12930 | 14193 | 11462 | 6525 |
| 21.64 | 16340 | 16052 | 13873 | 6840 |
| 22.26 | 16131 | 14989 | 13494 | 6313 |
| 22.97 | 16176 | 16093 | 14668 | 6581 |
| 23.85 | 16740 | 16515 | 14495 | 6561 |
| 24.54 | 16549 | 16079 | 14607 | 6599 |

background components: the sky + telescope background and the light provided by the non resolved stars + the contribution due to the superposition of the very extended halos of the individual sources. While the former gets brighter at longer wavelengths, the latter is more important when the SR is lower (i.e. at shorter wavelengths), and when the crowding is higher.

Matching the input and output catalogue allows us to determine the calibration constant for the output magnitudes as the average magnitude difference of the brightest stars (~ 300 objects). In Fig. 7 we compare the input and the output luminosity functions for five cases in the I and in the J bands. The luminosity functions are well recovered down to a magnitude which becomes progressively fainter as the crowding decreases (i.e. μ_B increases). The magnitude levels of 50 per cent completeness (expressed as the ratio between the output and the input luminosity functions) are shown in Fig. 8 as functions of the surface brightness. At

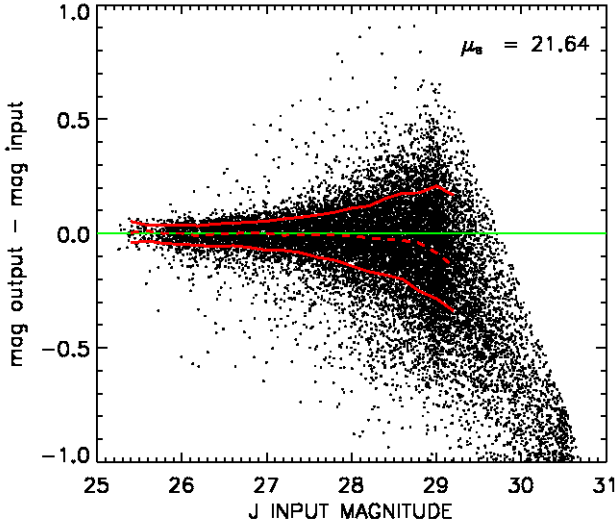


Figure 9. Comparison of the input and measured magnitudes of the matched stars for the case with $\mu_B = 21.64$ mag arcsec $^{-2}$ in the J band. The red solid lines show the 1σ widths of the errors distributions as function of input magnitudes, computed separately for the positive and negative sides. The curves are plotted up to the magnitude where the output catalogue becomes 50 per cent incomplete ($J \simeq 29.4$ mag). The dashed red line shows the median error.

$\mu_B \gtrsim 21.5$ mag arcsec $^{-2}$, the 50 per cent completeness magnitude becomes independent of the surface brightness in all bands, indicating that below this level, the source detection is no longer limited by crowding.

Another important aspect highlighted by Fig. 7 is the difference between the output luminosity function and the luminosity function of the input stars matched to the stars recovered by the data reduction. The two distributions coincide in the brightest bins, where photometry is very accurate, but below a certain magnitude, which depends on the crowding conditions, the output luminosity function typically exceeds the input one. This is due to blending which causes the migration of stars towards brighter bins along the luminosity function (see, e.g., Greggio & Renzini 2011).

The photometric error is illustrated in Fig. 9 where we compare the input and measured magnitudes of the matched stars for the case with $\mu_B = 21.64$ mag arcsec $^{-2}$ in the J band. The median value of the magnitude difference is zero for the brightest stars (by construction), but becomes progressively more negative going towards fainter magnitudes. For each star, the photometric error is due to both crowding and noise. While the noise causes a randomly distributed error in the direction of brighter or fainter magnitudes, the crowding leads to a negatively biased error, pushing the stars more frequently into brighter bins. This is the reason for the asymmetrical distribution of the magnitude differences in Fig. 9. The 1σ width loci are compared in Fig. 10 for various values of the surface brightness (i.e. crowding conditions) in different bands. It is apparent that in the case of $\mu_B = 19.3$ mag arcsec $^{-2}$ the photometric accuracy is rather poor at all wavelengths. The error distribution appears very asymmetrical due to blending, especially in the more crowded

regions. Notice that the photometric accuracy in the I band is similar to that in the Near-IR bands, in spite of the worse AO correction quality (i.e. lower SR) at shorter wavelengths. This is due to the lower sky background in the optical. Similar level of completeness and values for the photometric errors have been reported by Deep et al. (2011).

4.2 Color Magnitude Diagrams

CMDs have been obtained by combining the catalogues in the four broad-band filters (I , J , H and K_s) for each of the 8 cases in Table 2. Fig. 11 shows the output (J , $I - J$), (H , $I - H$) and (J , $J - K$) CMDs at four surface brightness levels, covering a range between $19.3 \leq \mu_B \leq 23.85$ mag arcsec $^{-2}$, that corresponds to a radial range of $0.1 \leq R/Reff \leq 1.5$ for a typical bright elliptical galaxy. In each panel of Fig. 11 dashed lines show the 50 per cent completeness limits in the two bands used to construct the CMD. It appears that the adopted exposure times allow us to derive complete CMDs in the external regions at $\mu_B > 21.6$ mag arcsec $^{-2}$, and that the limits in the I , J and H bands are equivalent for sampling the RGB stellar population. The limiting magnitude in the K_s band appears instead too bright compared to that in the J band, as shown by the lack of stellar detections at $K_s \gtrsim 27.5$ mag in the bottom right panel of Fig. 11, which are detected in the J band. However, the (J , $J - K$) diagrams still sample the upper 2 magnitudes of the RGB with high completeness factors, which should suffice for the determination of the MDF.

The effect of crowding on photometric accuracy can be appreciated on Fig. 11 as an increasing depth and better color separation as the surface brightness becomes fainter. Notice that the separation of the different colors on the CMDs reflects the separation of stars in different metallicity bins, thus tracing our ability to derive the metallicity distribution from the color distribution of the stars. In the most crowded regions the background is amplified by the large amount of unresolved stars with their very extended PSF halos. This effect is more pronounced in the bands where the sky and instrument background is not dominant. In addition, the accuracy of the PSF strongly worsens with increasing crowding. These factors produce the high incompleteness and large scatter on the observed CMD in the high surface brightness cases. Below $\mu_B \simeq 21.6$ mag arcsec $^{-2}$ completeness levels remain the same, while color separation continues to improve towards fainter surface brightness levels. We also notice that the Tip of the RGB is badly defined in the most crowded cases, due to the effect of blending which causes a spurious brightening of the stars just below the RGB Tip.

All combinations of the photometric bands sufficiently sample the bright RGB (red) stars. However, the color separation of stars with different metallicities is much better achieved in CMDs that include the I band. Indeed, this allows a wider wavelength baseline which more effectively traces the effective temperature of the RGB stars. In spite of the best AO correction, the K band is less efficient than other infrared bands because of the high background which limits the depth and the accuracy of the K_s band detections. Therefore the photometric metallicity is better determined using the $I - J$ or the $I - H$ colors. Both options (obtained with the same exposure times) look very similar from the quality of the CMDs shown in Fig. 11. For this reason, in the

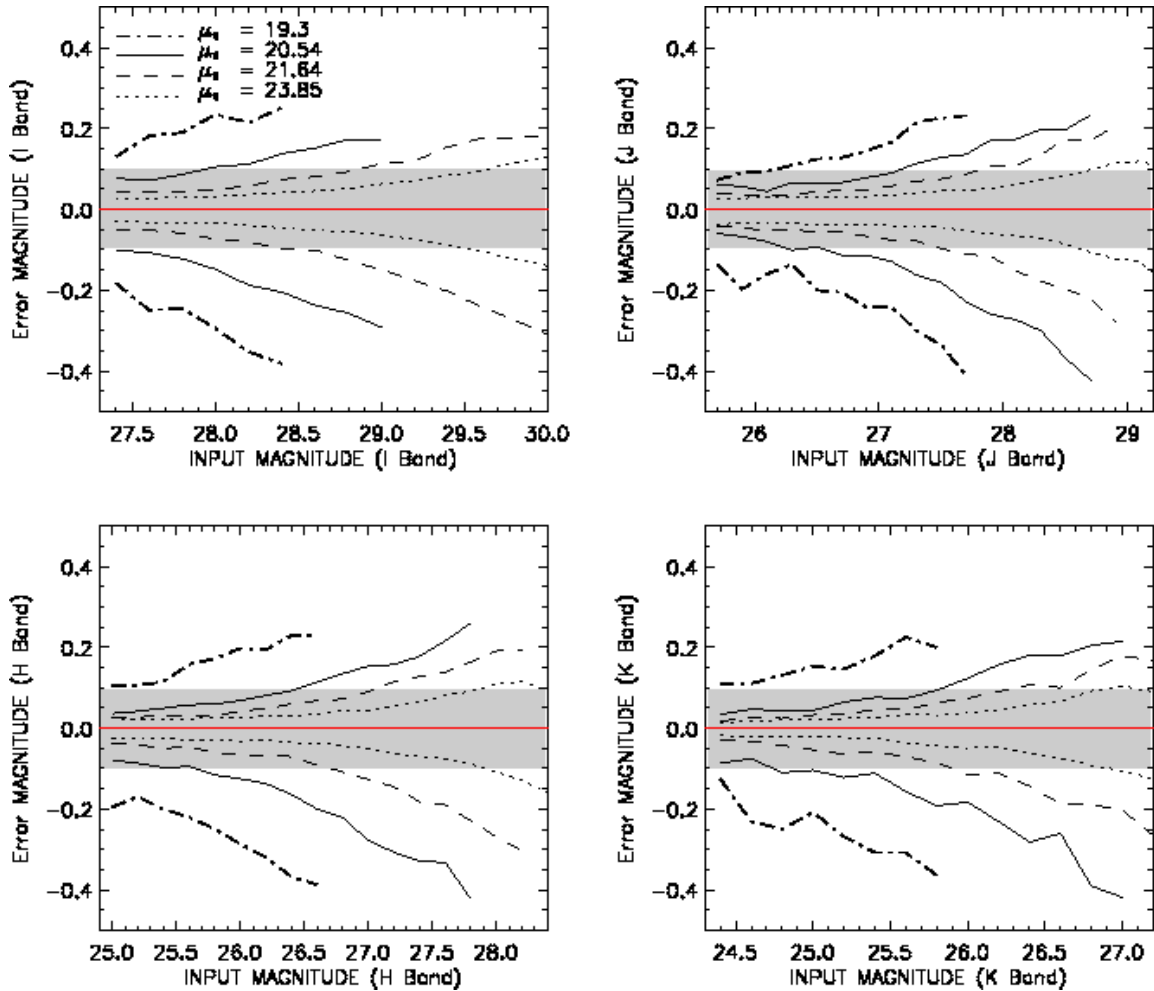


Figure 10. Photometric errors as a function of the input I (top left), J (top right), H (bottom left) and K_s (bottom right) magnitudes. The different line styles are associated with different surface brightness values, as labeled in the top right panel. The curves are plotted up to the magnitude where the output catalogue becomes 50% incomplete. The shaded gray stripes highlight the region of the plots where the error is $-0.1 \leq \sigma \leq 0.1$ mag. A photometric error of $\sigma \sim 0.1$ mag is reached at $I \simeq 28$, $J \simeq 27.1$, $H \simeq 26.4$ and $K_s \simeq 25.8$ mag in the $\mu_B = 20.54$ mag arcsec $^{-2}$ case, while is reached at $I \simeq 29.6$, $J \simeq 28.7$, $H \simeq 27.9$ and $K_s \simeq 26.9$ mag in the $\mu_B = 23.85$ mag arcsec $^{-2}$ case. In the $\mu_B = 20.54$ mag arcsec $^{-2}$ case an error of $\sigma \sim -0.1$ mag is reached at $I \simeq 27.5$, $J \simeq 26.5$, $H \simeq 25.7$ and $K_s \simeq 25$ mag.

following we consider only the J vs $I - J$ CMD to evaluate the impact of crowding on the derivation of the metallicity distribution from the photometry of the RGB stars.

4.3 Metallicity Distribution Function

Since the determination of the metallicity relies on the color of the stars, it is important to analyze the error on the colors of the detected sources. Fig. 12 shows the r.m.s. on the color of the detected (and matched) stars for two different cases of crowding. As already mentioned the crowding leads to a negatively biased error at all wavelengths. This asymmetrical distribution of the photometric error is well described by the trend of the median photometric error depicted in Fig. 12 and by the asymmetrical distribution of the photometric error curves depicted in Fig. 10. This error source at different wavelength is statistically correlated. For this reason, when combining photometric mea-

surements of different bands to recover the color of the stars, this statistically correlated component of the photometric errors does not sum in quadrature, but partially compensates (Olsen, Blum & Rigaut 2003). As a result, for highly crowded fields, the smaller than that of individual photometric measurements. This interesting effect is well depicted in Fig. 12. The situation is different in low crowding conditions, where the photometric error is dominated by the photon noise: in this case the errors in the two bands are uncorrelated and, therefore, the error on the color is similar (or larger) to that of the photometry in a single band. Similar considerations hold when comparing the error on the color to that of the individual magnitude in the J band.

We now turn to examine the metallicity distribution derived from the single star photometry as a function of crowding conditions. The photometric metallicity is determined by comparing the position of the measured stars to model loci characterized by different values of the metallicity. As

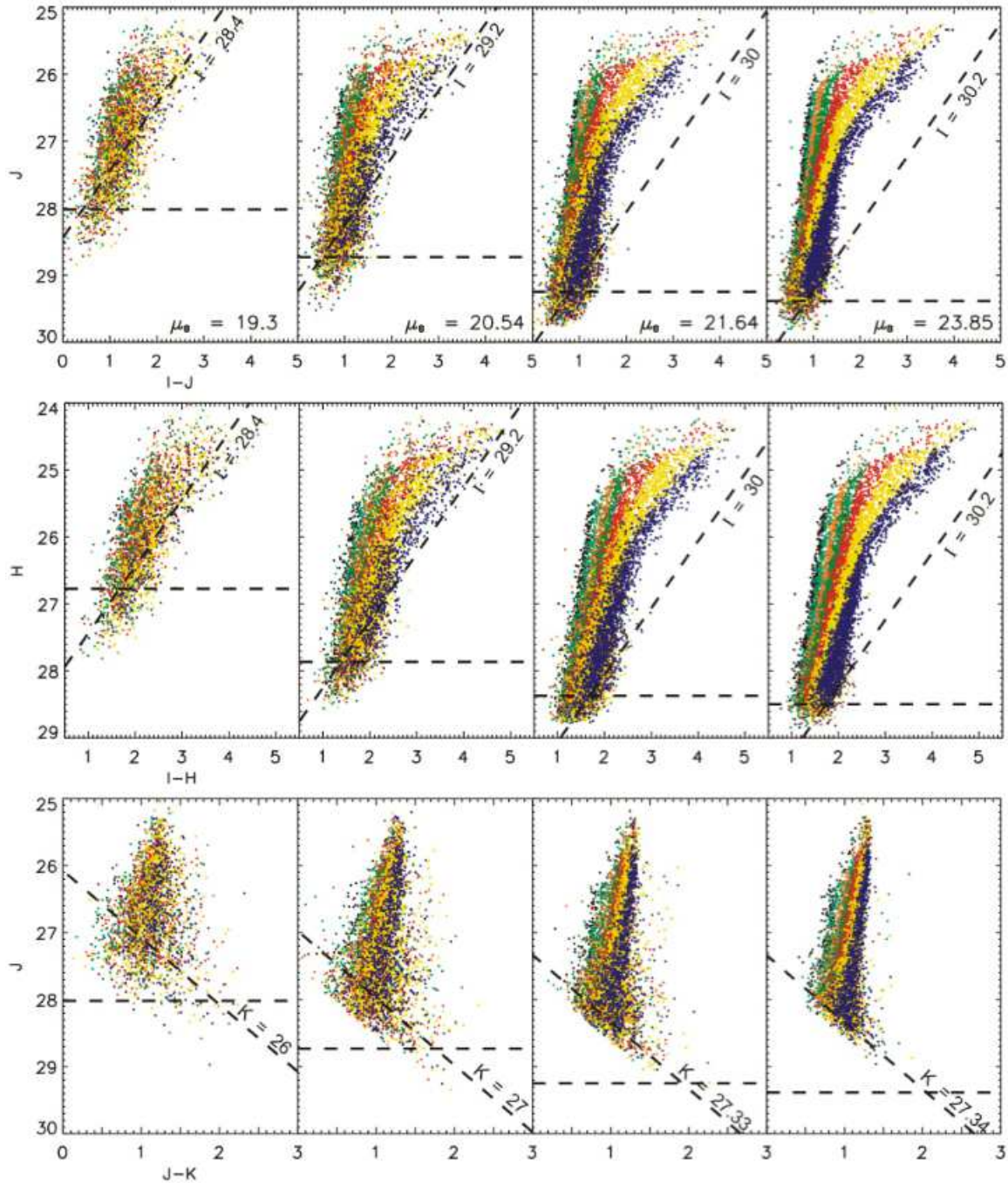


Figure 11. Output ($J, I - J$) (upper panels), ($H, I - H$) (central panels) and ($J, J - K$) (lower panels) CMDs for different surface brightness levels as labeled. The color reflect the metallicity bin of the object with the same encoding as on Fig. 1. The metallicity of the output stars is identified on the basis of the positional coincidence with input objects on the J band image for the ($J, I - J$) and ($J, J - K_s$) CMDs and on the H band image for the ($H, I - H$) CMD. The dashed lines highlight the 50 per cent completeness in the two colors.

underlined in the introduction, this method is subject to uncertainties related to the age-metallicity degeneracy and to the AGB contribution to the counts in this part of the CMD (see, e.g., Gallart et al. 2005). For example, Rejkuba et al. (2011) show that neglecting the AGB contribution when deriving the MDF from this portion of the CMD leads to

underestimating the average metallicity of the population, since AGB stars are bluer than their RGB progenitors. This effect, however, is small and can be easily accounted for with simulations based on evolutionary tracks. More insidious is the age-metallicity degeneracy for which RGB stars have the same color for age and metallicity combinations with higher

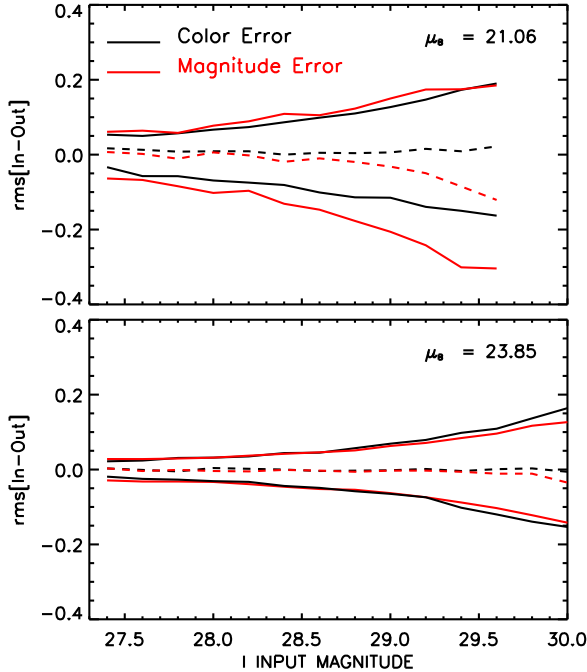


Figure 12. 1σ photometric errors on the I band magnitude (red lines) and on the $I - J$ color (black lines) a function of the input I magnitude. The error on $I - J$ is computed as the color difference of stars positionally matched on the I band image. The positive and negative 1σ widths of the errors distributions have been computed separately. The dashed lines show the median errors. The two panels illustrate the trends for two different surface brightness levels.

metallicity at younger ages. For old stellar populations (age $\gtrsim 8$ Gyr), simulations based on stellar tracks indicate that the MDF derived with this method shifts to metallicities higher by ~ 0.1 dex when the age is assumed younger by ~ 3 Gyr.

Besides these systematic effects, the photometric errors introduce an additional uncertainty that is investigated with our simulated frames. The main aim of this paper is to quantifying this additional uncertainty and its systematic with crowding, while establishing the reliability of the metallicity derived with the photometric method is beyond our scope. Fig. 13 shows the theoretical loci adopted for our exercise, derived from the simulated CMD shown in Fig. 1, by dividing the list of input stars in metallicity bins, and computing the average $I - J$ color as function of the J magnitude for the various bins. The theoretical lines include the effect of the AGB component by construction. The metallicity of each detected star in our *observed* CMD is then derived by interpolation on this grid. This is equivalent to the method applied in Rejkuba et al. (2011) to HST data to derive the metallicity distribution in a halo field of the elliptical galaxy Cen A.

For the stars which have been positionally matched to an input object two values of the metallicity are determined: one is the true metallicity of the input star ($[\text{Fe}/\text{H}]_i$), and the other is the observed metallicity derived from the interpolation described above ($[\text{Fe}/\text{H}]_o$). The difference between

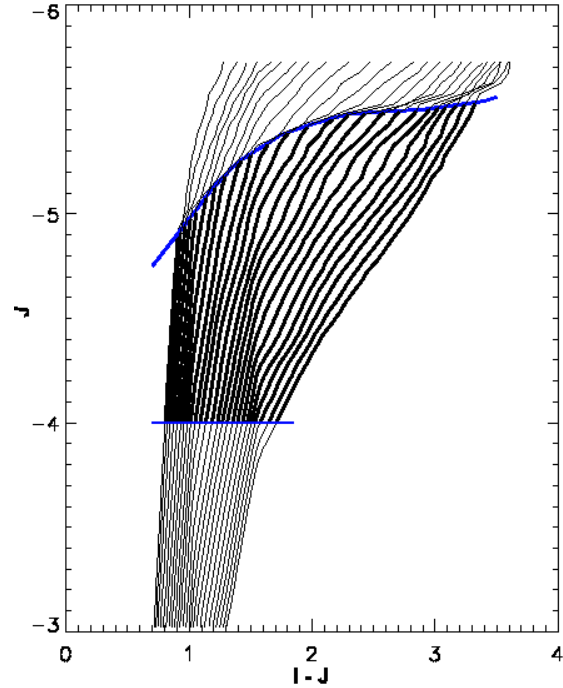


Figure 13. Theoretical isometallicity loci ($-1.5 \leq [\text{Fe}/\text{H}] \leq 0.16$, with a step size ranging between 0.1 and 0.04 dex) obtained from the simulated $(I, I - J)$ CMD by averaging the color as a function of the J magnitude for the various bins. The portion in boldface shows the section of the CMD used to determine the photometric metallicity for all our considered cases.

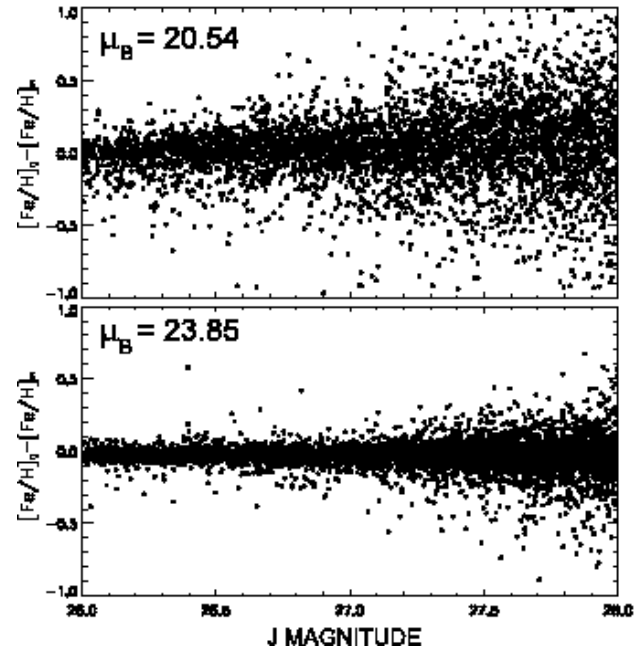


Figure 14. Error on the metallicity determination induced by the photometric scatter on the CMD as a function of the J magnitude for two levels of surface brightness.

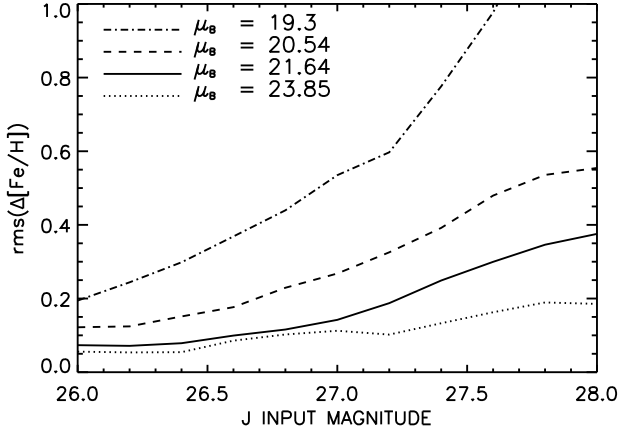


Figure 15. Variation of the r.m.s. of the $\Delta[\text{Fe}/\text{H}]$ of individual stars with the J magnitude for various surface brightnesses.

these two values represents the error on the metallicity induced by the photometric scatter on the CMD. Fig. 14 plots this error as a function of magnitude for two of our considered cases. This error is clearly higher for the more crowded field, and it increases as stars become fainter. Fig. 15 exemplifies these trends showing the r.m.s. of the distribution of the errors on metallicity ($\Delta[\text{Fe}/\text{H}] = [\text{Fe}/\text{H}]_o - [\text{Fe}/\text{H}]_i$) as a function of the magnitude for various surface brightness levels.

To determine the photometric metallicity distribution we restrict the analysis to a sub-sample of the measured stars, selecting only the portion shown in boldface on Fig. 13. This is limited by the Tip of the RGB on the bright side, since we prefer avoiding the region populated only by AGB stars. The lower limit to the luminosity is instead used to delimit a portion of the CMD where the sensitivity of the color to the metallicity is relatively high.

Fig. 16 compares the input metallicity distribution to the one derived with this method for the four levels of surface brightness. We notice that the photometrically derived distribution is slightly overpopulated on the low metallicity side of the peak. The overall shape of the two distributions, however, is quite similar in all the examined cases, provided that the binning is wider in the most crowded fields. The accuracy with which the MDF is recovered, as mapped by the width of the bins in Fig. 16, worsens towards the inner regions, as does the photometric quality. Actually we find an almost linear relation between the error at relatively faint magnitudes and the width of the optimal metallicity bin.

We conclude that the metallicity distribution can be recovered with a resolution better than 0.2 dex in a Virgo Elliptical in regions with a surface brightness fainter than $\mu_B \simeq 21.6$ mag arcsec $^{-2}$. The magnitude of this uncertainty is of the same order as that related to the age-metallicity degeneracy.

5 EFFECT OF PSF VARIATIONS

The cases illustrated so far (hereafter referred to as case A) adopt the PSF computed at the center of the MICADO FoV, where the MCAO correction is more efficient, and in “good

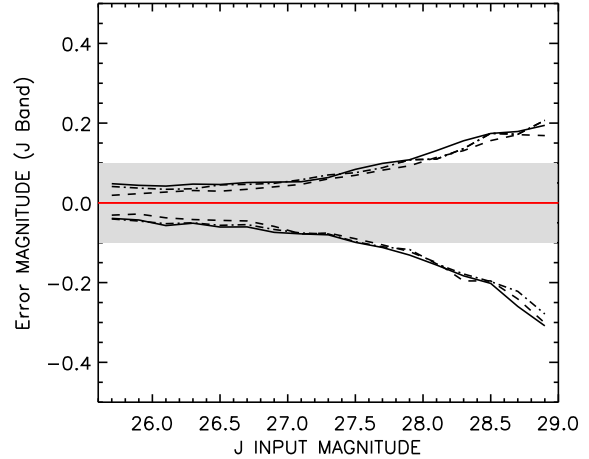
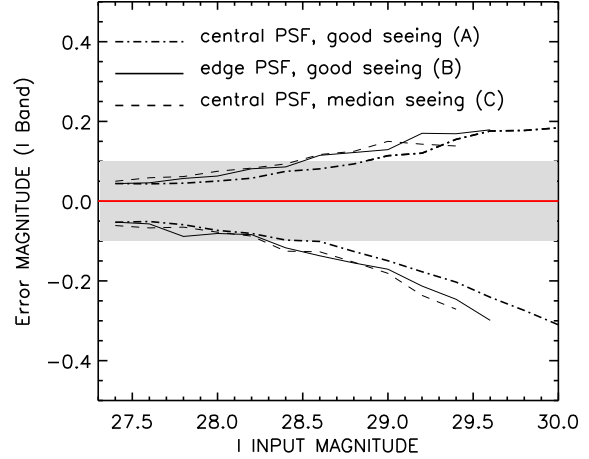


Figure 17. Photometric errors as a function of the input I (top panel) and J (lower panel) magnitudes. The different line styles are associated with different input PSFs. The curves are plotted up to the magnitude where the output catalogue becomes 50 per cent incomplete. The shaded stripes highlight the region of the plots where the error is $-0.1 \leq \sigma \leq 0.1$ mag. An error of $\sigma \sim 0.1$ mag is reached at $I \simeq 29, 28.7$ and 28.5 mag and $J \simeq 28.1, 28.05$ and 28 mag for A, B and C cases respectively, while an error of $\sigma \sim -0.1$ mag is reached at $I \simeq 28.4, 28.3$ and 28.3 mag and $J \simeq 27.6$ mag for all the cases.

seeing” condition. In order to characterize the impact of the PSF variation on our science case we computed two more sets of simulations adopting different PSFs. To test the effect of spatial variation of the PSF on the MICADO FoV we generated frames adopting the PSF at the edge of the FoV and “good seeing” (blue point in Fig. 3, hereafter case B). We test the effect of seeing adopting the central PSF under “median seeing” conditions (hereafter case C). The main characteristics of the three considered PSFs are listed in Table 5. These cases correspond to considering a degradation of the PSF SR (see Fig. 4), but also variations of the PSF shape, especially in the halo substructure (see Fig. 2.3). For this experiment we selected one of the cases in Table 2, i.e. the case at $0.5 R_{\text{eff}}$ (with $\mu_B = 21.64$ mag arcsec $^{-2}$), which appears to represent the limit beyond which the photometric accuracy becomes almost insensitive to crowding. The analysis has been carried out for the I and J bands follow-

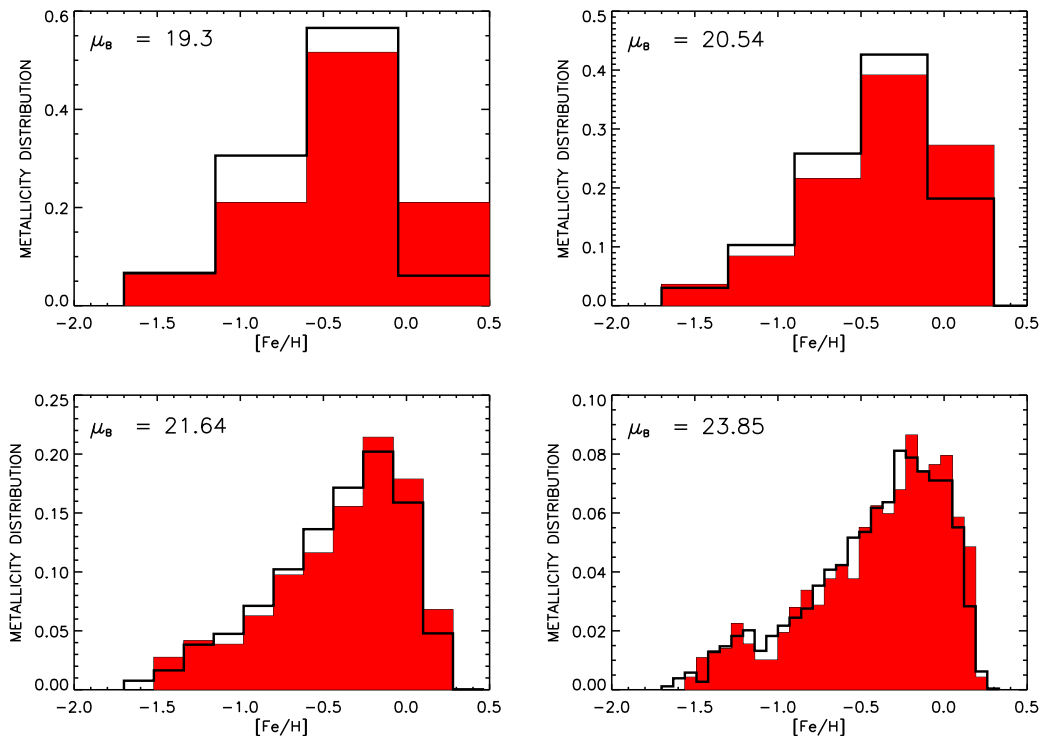


Figure 16. Input (red filled histogram) and recovered (black thick histogram) metallicity distributions. The $[\text{Fe}/\text{H}]$ bins have been adjusted in order to bring the input and the output histograms into best agreement, e.g. so that the peaks coincide. The bin widths are respectively of 0.55, 0.4, 0.18, 0.07 dex for $\mu_B = 19.3, 20.54, 21.64$ and 23.85 mag arcsec $^{-2}$.

Table 5. Summary of the characteristics of the PSFs used to generate the analyzed frames. The values of the SRs for each case can be extrapolated from Fig. 4.

| Case | PSF position in the FoV ($X;Y$)'' | SR seeing | SR I band | SR J band |
|------|---|--------------|----------------|----------------|
| A | (0;0)'' | 0.6'' | 0.06 | 0.22 |
| B | (23;19.3)'' | 0.6'' | 0.042 | 0.17 |
| C | (0;0)'' | 0.8'' | 0.03 | 0.16 |

ing the same steps illustrated in previous Sections. The SR degradation influences the number of detected sources, especially in the I band where the AO correction is poorer, leading to a brighter detection limit for cases B and C compared to A. The correlation between the detection limit and the SR (which impacts on the signal to noise ratio) is apparent comparing the 50 per cent completeness magnitudes reported in Table 6 with the SR values reported in Table 5.

Fig. 17 illustrates the photometric quality as a function of the input magnitudes in the I and J bands. We recall that the surface brightness (i.e. crowding) is fixed. Note that the error curves for the three cases almost overlap along the whole magnitude range in both bands. Indeed the accuracy of the PSF extraction is more affected by the crowding rather than the SR. A marginal increase of the negative error in cases with lower SR (B and C) can be noticed at faint I magnitudes ($I \gtrsim 29$ mag). This is probably due to the en-

Table 6. I and J magnitudes where the output luminosity functions, computed for $\mu_B = 21.64$ mag arcsec $^{-2}$ and assuming different PSFs, become 50% incomplete. The PSFs characteristics of the three cases are listed in Table 5.

| Case | I mag | J mag |
|------|---------|---------|
| A | 30.0 | 29.2 |
| B | 29.5 | 29.0 |
| C | 29.3 | 28.9 |

hancement of the blending effect whereby a larger fraction of the flux is contained within the PSF halo.

The above considerations reflect into the $(J, I - J)$ CMDs appearance of the three cases shown in Fig. 18. The effect of the SR degradation on the color separation of different metallicity bins seems to be negligible, while it affects significantly the CMDs depth. Fig. 20 compares the input metallicity distribution to the one derived following the procedure described in Sect. 4.3 for cases B and C. We found that the overall shape of the two distributions is again quite similar. Even the r.m.s. of the errors on the metallicity estimation as a function of magnitude (colored lines in Fig. 19) in cases B and C are slightly larger with respect to case A, but comparable within ~ 0.05 dex.

We may conclude that the considered cases of PSF SR degradation do not influence the accuracy with which we can recover the MDF in a Virgo Elliptical in regions with a surface brightness fainter than $\mu_B \simeq 21.6$ mag arcsec $^{-2}$. This confirms the feasibility of our science case.

6 SUMMARY AND CONCLUSIONS

In this paper we investigated the expected performance reached by next generation large aperture telescopes for the photometric study of resolved stellar population in distant galaxies. This work focus on the capabilities of deriving the metallicity distribution of stellar populations in distant galaxies using the future E-ELT high resolution imager MICADO. In particular we quantified the impact of the photometric errors on the metallicity distribution derived from the color distribution of RGB stars, and of its systematics with different crowding conditions. This uncertainty is in addition to that related to the age-metallicity degeneracy and inadequacies of the stellar evolutionary tracks. We have shown that the exquisite spatial resolution offered by the E-ELT working close to the diffraction limit, will allow us to perform accurate photometry of bright RGB stars in extremely crowded fields, down to the inner regions of galaxies. It will be therefore possible to map the metallicity distribution across practically an entire elliptical galaxy, with a modest resolution (~ 0.5 dex) in the central regions. At larger radii the resolution improves, becoming ~ 0.1 dex at the effective radius and even better in the external regions.

We produced synthetic frames in the I , J , H and K_s bands at different surface brightness levels ($19.3 \leq \mu_B \leq 24.54$) assuming the expected PSF of the MICADO camera assisted by the MAORY MCAO module. We used different PSFs computed under different assumptions of seeing conditions and AO performance across the MICADO FoV.

The generated frames have been analyzed using StarFinder, a program specifically designed for high resolution AO images.

The photometric accuracy has been evaluated for each band and for each crowding condition, matching the input and output stellar lists. As in Greggio et al. (2012), we found that blending of stellar sources in most crowded fields leads to an asymmetrical error distribution, and to a general migration of star counts along the luminosity function towards the brighter bins. Our analysis has shown that:

- stellar photometry in crowded fields of distant galaxies is feasible with an accuracy of $\sigma \simeq 0.1$ mag at $\simeq 0.5 R_{\text{eff}}(\mu_B = 21.6 \text{ mag arcsec}^{-2})$ and with an accuracy of $\sigma \simeq 0.2$ mag at $\simeq 0.25 R_{\text{eff}}(\mu_B = 20.5 \text{ mag arcsec}^{-2})$ down to $J \simeq 27.7$ mag. This allows studies of resolved stellar populations in the inner regions of elliptical galaxies up to the distance of the Virgo cluster;
- the luminosity function on the upper two magnitudes of the RGB is well determined for surface brightness levels fainter than $\mu_B \simeq 20.5 \text{ mag arcsec}^{-2}$ (corresponding to $\simeq 0.25 R_{\text{eff}}$);
- at $\mu_B \sim 21.6 \text{ mag arcsec}^{-2}$ the completeness becomes independent of surface brightness in all the bands, indicating that below this level, the source detection is no longer limited by crowding;
- the photometric errors introduce an uncertainty ≤ 0.2 dex in the determination of the peak of the metallicity distribution in regions with a surface brightness fainter than $\mu_B \simeq 21.6 \text{ mag arcsec}^{-2}$; at this surface brightness level the photometric errors for stars brighter than $J \simeq 27$ mag induce a typical accuracy of ~ 0.1 dex on the photometric metallicity;
- when considering a non optimal PSF, such as the one

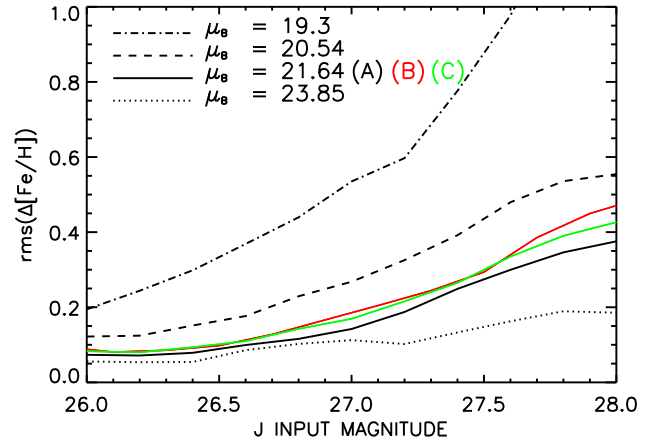


Figure 19. Variation of the r.m.s. of the $\Delta[\text{Fe}/\text{H}]$ of individual stars with the J magnitude for various surface brightness. In the case of $\mu_B = 21.64 \text{ mag arcsec}^{-2}$ we also reported the curves assuming different PSFs. The block capital letters A, B and C refer respectively to frames simulated assuming: A) PSF at the center of the MICADO FoV and seeing = 0.6 arcsec (as shown in Fig. 8); B) PSF at the center of the MICADO FoV and seeing = 0.8 arcsec; C) PSF at the edge of the MICADO FoV and seeing = 0.6 arcsec.

obtained in worse seeing condition or at the edge of the imaging camera FoV, it is still possible to retrieve the metallicity distribution with an accuracy similar to the one recovered assuming the best PSF, while the CMDs become less deep.

ACKNOWLEDGMENTS

L.S. acknowledges the support of INAF through the 2011 postdoctoral fellowship grant. This work has been partially supported by the T-REX project (*Progetto Premiale T-REX*). L.S. wants to thank Emiliano Diolaiti (INAF - Osservatorio Astronomico di Bologna) for its essential suggestions and support in the data reduction. L.S. thanks also Antonio Sollima (INAF - Osservatorio Astronomico di Bologna) for the support and the useful discussions.

REFERENCES

- Beckers J. M., 1993, *ARA&A*, 31, 13
 Ciotti L., Lanzoni B., & Volonteri M., 2007, *ApJ*, 658, 65
 Ciotti L., 2009, *Nature*, 460, 333
 Coccatto L., Arnaboldi M., Gerhard O., et al., 2010, *A&A*, 519, A95
 Crnojević D., Ferguson A. M. N., Irwin M. J., et al., 2013, *MNRAS*, 432, 832
 Davies R. et al., 2010, *Proc. SPIE*, 7735, 77
 Diolaiti E., Bendinelli O., Bonaccini D., et al., 2000, *Proc. SPIE*, 4007, 879
 Diolaiti E., Conan J.-M., Foppiani I., et al., 2010, *Proc. SPIE*, 7736
 Deep A., Fiorentino G., Tolstoy E., Diolaiti E., Bellazzini M., Ciliegi P., Davies R., Conan J.-M., 2011, *A&A*, 531, A151

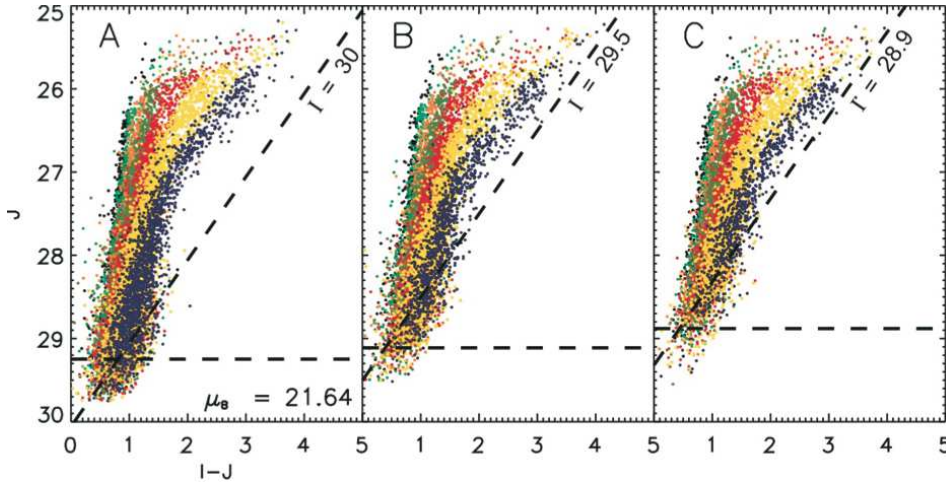


Figure 18. Output ($J, I - J$) CMDs in the same crowding conditions ($\mu_B = 21.64 \text{ mag arcsec}^{-2}$) assuming three different input PSFs. The color reflects the metallicity bin of the object with the same encoding as on Fig. 1. The metallicity of the output stars is identified on the basis of the positional coincidence with input objects on the J band image. The dashed lines highlight the 50 per cent completeness in the two colors.

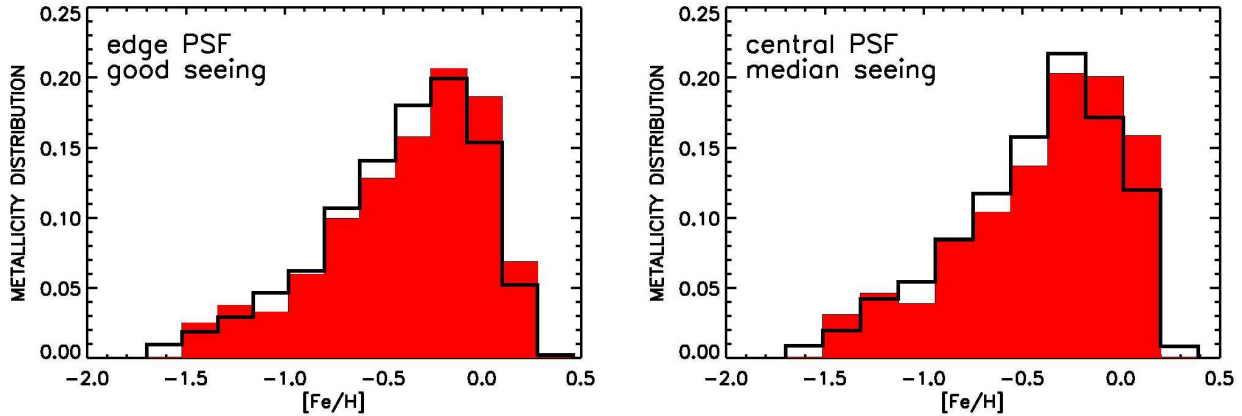


Figure 20. Input (red filled histogram) and recovered (black thick histogram) metallicity distributions for the non-optimal PSFs cases considered and $\mu_B = 21.64 \text{ mag arcsec}^{-2}$. The $[\text{Fe}/\text{H}]$ histogram bin widths for which the input and output metallicity distributions are in best agreement are 0.18 and 0.19 dex for cases B and C respectively, c.f. the 0.18 bin width of case A (Fig. 16).

Falomo R., Fantinel D., Uslenghi M., 2011, Proc. SPIE, 8135, 813523
 Fiorentino G., Tolstoy E., Diolaiti E., et al., 2011, A&A, 535, A63
 Gallart C., Zoccali M., & Aparicio A., 2005, ARA&A, 43, 387
 Girardi L., Bertelli G., Bressan A., et al., 2002, A&A, 391, 195
 Gilmozzi R., Spyromilio J., 2007, The Messenger, 127, 11
 Gullieuszik M., Greggio L., Held E. V., et al., 2008, A&A, 483, L5
 Greggio L., Renzini A., 2011, Stellar Populations. A User Guide from Low to High Redshift., Wiley-VCH Verlag-GmbH & Co. KGaA, Weinheim, Germany
 Greggio, L., Falomo, R., Zaggia, S., Fantinel, D., & Uslenghi, M. 2012, PASP, 124, 653
 Harris G. L. H., Harris W. E., & Poole G. B., 1999, AJ, 117, 855

Harris G. L. H., & Harris W. E., 2000, AJ, 120, 2423
 Herriot G., Andersen D., Atwood J., et al., 2010, Adaptive Optics for Extremely Large Telescopes, edited by Y. Clnet, J.-M. Conan, T. Fusco and G. Rousset, published by EDP Sciences
 Kim D., & Im M., 2013, ApJ, 766, 109
 Kormendy J., Fisher D. B., Cornell M. E., & Bender R., 2009, ApJS, 182, 216
 Marchetti E., Brast R., Delabre B., et al., 2008, Proc. SPIE, 7015
 Neichel B., Rigaut F., Bec M., et al., 2010, Proc. SPIE, 7736
 Olsen K.A.G., Blum R.D., Rigaut F., 2003, AJ, 126, 452
 Oser L., Ostriker J. P., Naab T., Johansson P. H., & Burkert A., 2010, ApJ, 725, 2312
 Rawle T. D., Smith R. J., & Lucey J. R., 2010, MNRAS, 401, 852
 Rejkuba M., Greggio L., Harris W.E., Harris G.L.H., Peng

- E.W., 2005, AJ, 631, 262
Rejkuba M., Harris W.E., Greggio L., Harris G.L.H., 2011, A&A, 526, A123
Rigaut F., Neichel B., Boccas M., et al., 2012, Proc. SPIE, 8447
Schreiber L., Diolaiti E., Sollima A., et al., 2012, Proc. SPIE, 8447
Szeto K., et al., 2008, Proc. SPIE, 7012, 86
Weijnans A., Cappellari M., Bacon R., de Zeeuw T.P., Emsellem E., Falcon-Barroso J., Kuntschner H., McDermid R.M., van den Bosch R. C.E., van de Ven, G., 2009, MNRAS 398, 561

This paper has been typeset from a \TeX / \LaTeX file prepared by the author.